Multi-Fidelity Shape and Mission Optimization Including Transient Thermal Constraints

Christopher A. Lupp & Daniel L. Clark, Jr.
Air Force Research Laboratory
Wright-Patterson Air Force Base
UNITED STATES

Christopher T. Aksland
University of Illinois Urbana-Champaign
Champaign, Illinois
UNITED STATES

Andrew G. Alleyne
University of Minnesota Twin Cities
Minneapolis, Minnesota
UNITED STATES

Keywords: Multi-Fidelity, Multidisciplinary Design Optimization, Shape Optimization, Power and Thermal Management System Design, Trajectory Optimization

ABSTRACT

The co-design of aircraft, their subsystems, and their mission profile presents an opportunity to obtain higher performance vehicles tailored for their intended missions. In particular, the effect of the Power and Thermal Management System (PTMS) can have a significant impact on mission performance. Therefore, the vehicle's aerodynamic shape, its PTMS sizing, and mission trajectory are closely coupled and simultaneous optimization may yield significant performance gains. However, running high-fidelity aerodynamic analyses for the transient solution is computational intractable. A multi-fidelity approach, using lower fidelity aerodynamic analyses for the transient solutions, offers a potential solution. This paper explores the coupling of these three disciplines for a transient optimization problem. The coupled design process is illustrated using a hybrid-electric High Altitude Long Endurance (HALE) aircraft. Both a sequential and fully coupled design are conducted and the results compared. Finally, the accuracy of the aerodynamic model at varying fidelity is assessed.

NOMENCLATURE

D	drag force, N
I_{sp}	specific impulse, s^{-1}
L	lift force, N
T	thrust force, N
g	gravitational acceleration, $\frac{m}{s^2}$

h geodesic altitude, m

m aircraft mass, kg

r horizontal distance, m

v airspeed, $\frac{m}{s}$

x_{shear} mesh deformation in x-direction

y_{PTMS} states associated with the PTMS

C_D drag coefficient

C_L lift coefficient

C_{D0} min. drag coefficient

C_{L0} lift coefficient at $\alpha = 0$

α angle of attack, $^\circ$

γ flight path angle, $^\circ$

k induced drag factor

η duty cycle

T_i spline control points for the thrust

γ_i spline control points for the flight path angle

τ_{gen} generator torque, Nm

ϑ_∞ ambient temperature, °C

ϑ_i PTMS component temperatures, °C

$()^i$ initial quantity

$()^*$ optimal quantity

1 INTRODUCTION

The co-design of vehicles, their subsystems, and mission profiles presents an opportunity to obtain higher performance designs more closely tailored to their intended use. One avenue for increasing overall vehicle performance is to simultaneously size the aircraft's aerodynamic shape, power and thermal management system (PTMS), and mission trajectory. Past work by Jasa and coworkers [1] illustrates the value of coupled thermal and trajectory optimization as high speed vehicles may encounter problems with heat dissipation [2]. While thermal issues have long been primarily associated with supersonic and hypersonic vehicles, new electrical components that require short bursts of power may change the thermal management requirements of a vehicle [3]. Similarly,

recent interest in electric propulsion requires the design of these vehicles to account for thermal management and its coupling to the mission profile [4]. Thermal constraints may therefore pose limitations on aircraft performance that may be mitigated by including the mission-PTMS coupling in vehicle design optimization.

In past work, Alyanak and Allison [5] developed a method for determining thermal load constraints during conceptual design and found that varying the thermal system architecture may result in large performance differences of the aircraft. Falck and coworkers [4] conducted a gradient-based trajectory optimization including thermal constraints for NASA's X-57 aircraft. They demonstrated the ability to efficiently conduct aircraft trajectory optimization subject to thermal constraints on the propulsion system. Furthermore, they determined, that a reduction in heat exchanger size adversely affect the aircraft performance. Futhermore, Jasa and coworkers [1] examined the effects of thermal constraints on the optimization of a supersonic aircraft. They created an aerodynamic surrogate model from RANS CFD data and modeled a recirculating thermal system to manage engine waste heat for a thermally limited trajectory optimization problem. Similar to other works, they found that the thermal constraints may limit vehicle performance if the thermal system is not considered during vehicle design. Finally, Clark and Abolmoali [6] studied the robust design of a thermal system using pseudo-spectral methods, gradient-based optimization and uncertainty quantification.

As a result, gradient-based optimization capabilities are needed that couple trajectory and thermal analyses. Central to that goal is the ability to obtain a transient solution with derivatives for this coupled mission analysis. Fundamentally, explicit or implicit time integration methods may be used. Implicit methods include collocation methods, such as Gauss-Lobatto [7] or Radau [8] methods. Collocation methods have been used successfully for transient, gradient-based optimization problems [1, 6, 9, 10, 11].

While much of the previous literature is limited to analyses, recent work has featured gradient-based optimization, notably studies by Jasa and coworker [1] as well as Falck and coworkers [9]. However, the thermal systems in these optimization studies were limited to simple PTMS models that cannot be scaled to complex systems. Furthermore, Falck's work relies on an empirical aerodynamic solution. Jasa, by contrast, ran computational fluid dynamics (CFD) solutions and created a surrogate model as a preprocessing step. The surrogate was then used to obtain aerodynamic loads during the transient analysis during the optimization solution. Neither Falck's nor Jasa's aerodynamic models is applicable to shape optimization and, as a result, aerodynamic shape optimization has been neglected until now.

While past work has eschewed shape optimization in transient thermal and mission optimization problems, a multi-fidelity approach to the aerodynamic analyses offers a potential solution. Computationally efficient aerodynamic analyses (such as low-fidelity representations or surrogates) are necessary to make the transient analysis tractable. However, these low-fidelity methods do not offer sufficient model detail to permit aerodynamic shape optimization. Employing a multi-fidelity approach, the lower-fidelity model may be derived from a higher fidelity source during the optimization (unlike the preprocessing steps in Jasa's [1] work).

Multi-fidelity approaches featuring a reduction in model fidelity for computational savings have been applied previously for aeroelastic optimization. Malcolm and Laird [12] derived a method for obtaining equivalent beam properties from a high-fidelity Finite Element Method (FEM) model, originally intended for analyzing wind turbines. While Malcolm and Laird did not apply their work to optimization, they posited that high-fidelity shell FEM models are applicable for stress analyses, yet beam models should be used for aeroelastic analyses, due to the prohibitive computational cost of the high-fidelity solution. Stodieck and coworkers [13] as well as Lupp and Cesnik [14] extended Malcolm's beam reduction work to obtain gradients for gradient-based optimization problems. The goal of this gradient-based reduction process was to enable the objective (typically weight or

fuel burn) as well as some constraints (e.g., stress) to be evaluated using the high-fidelity solutions, while using a beam-based nonlinear aeroelastic solution for constraints that would be computationally intractable using the high-fidelity solution. This application differs from the narrow meaning of "multi-fidelity" sometimes associated exclusively with surrogates that mix data from sources of varying fidelity (such as co-kriging). However, problems featuring fidelity reduction should also be considered multi-fidelity, as they enable the inclusion of objectives or constraints in the optimization problem that would otherwise be computationally infeasible and improve the accuracy of the overall solution (as the absence of an analysis due to computational cost may result in an infeasible design).

This paper examines the simultaneous optimization of an aircraft's aerodynamic shape, its propulsion and PTMS subsystems, as well as its mission profile. A multi-fidelity approach is used to reduce the higher-fidelity aerodynamic analysis to obtain a low-fidelity representation applicable to transient analyses, while preserving a model representation detailed enough for shape optimization. Furthermore, the PTMS analysis methodology presented in this work permits the modeling of complex subsystems that previously could not be modeled in gradient-based multidisciplinary design optimization (MDO). Sequential vehicle and PTMS designs as well as a coupled optimization are presented to study potential impacts a tightly coupled problem may have on the vehicle design process. Finally, the accuracy of the multi-fidelity aerodynamic representation is quantified to determine requirements and limitations of the presented work.

2 NUMERICAL METHODS

To study the co-design of vehicle shape parameters, its PTMS sizing, and mission profile, a variety of disciplines must be coupled, ranging from aerodynamic analyses, to power and thermal simulations. The open source, gradient-based MDO framework, OpenMDAO [15], is used to coupled the various disciplines, while Dymos [16] is used to solve the transient trajectory and optimal control problem. As high-fidelity aerodynamic analyses, such as CFD, into the transient solution would escalate the computational expense, the optimization is formulated as a multi-fidelity problem (Figure 1). This section describes the individual disciplines required for the co-design studies and their integration into the larger MDO problem.

2.1 Multi-Fidelity Aerodynamic Representation

The transient flight mechanics require aerodynamic forces, which are provided using low-fidelity analytical relationships to reduce computational expense. Lift and drag are determined from the vehicle's lift and drag coefficients, as well as the atmospheric density, vehicle speed, and lifting surface area:

$$L = \frac{\rho}{2} v^2 S C_L \tag{1}$$

$$D = \frac{\rho}{2} v^2 S C_D, \tag{2}$$

while analytical linear and quadratic approximations are used for the lift and drag coefficients, respectively:

$$C_L = C_{L\alpha}\alpha + C_{L0} \tag{3}$$

$$C_D = C_{D0} + kC_L^2. \tag{4}$$

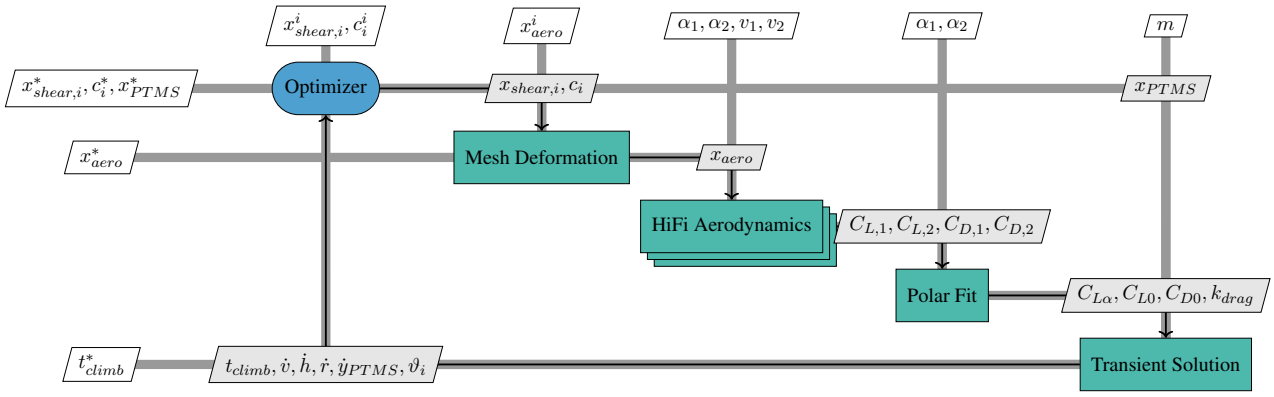

Figure 1: XDSM diagram [17] of the global multi-fidelity optimization problem, including the transient evaluation of the objective (climb time) and constraints (horizontal acceleration, component temperatures).

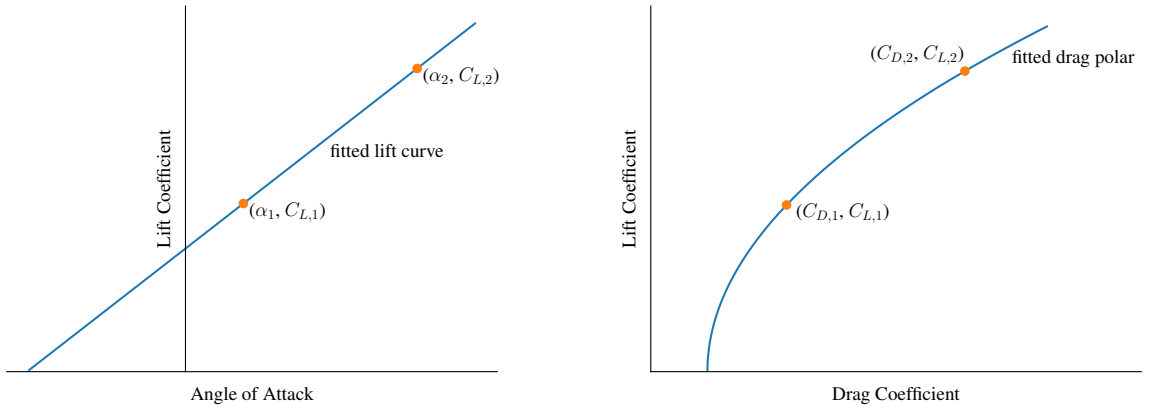

(a) Lift curve **(b) Drag polar**

Figure 2: Conceptual representation of the polar fitting required for the multi-fidelity optimization. As a linear function, the lift curve can be uniquely determined using two data points. While a generic second-order polynomial—used for the drag polar—requires three data points for a unique fit, the symmetry about the C_D-axis reduces that requirement to two data points.

This low-fidelity representation of the aerodynamic forces for the transient analysis is connected to higher-fidelity aerodynamic analyses—in this work OpenAeroStruct's vortex lattice method (VLM) solver [18] is used, however CFD or similar are conceivable alternatives—via a polar fit (Figure 2). The VLM analysis used is incompressible (no Prandtl-Glauert correction) and does not use viscid corrections. The high-fidelity solution (VLM) enables a spatial representation of the aerodynamic model (flat representation of lifting surfaces) which is not available

in the low-fidelity lift curve and drag polar. This permits coupling the geometric design variables (e.g., chord, controlled via 5 B-spline control points) to the transient solution.

For the lift coefficient, the fit is determined from two high-fidelity aerodynamic analyses, obtained from two equations with two unknown variables (C_{L0} and $C_{L\alpha}$):

$$C_{L,1} = C_{L\alpha}\alpha_1 + C_{L0} \tag{5}$$
$$C_{L,2} = C_{L\alpha}\alpha_2 + C_{L0}. \tag{6}$$

Therefore, the resulting coefficients for the lift curve are:

$$C_{L\alpha} = \frac{C_{L,2} - C_{L,1}}{\alpha_2 - \alpha_1} \tag{7}$$
$$C_{L0} = C_{L,1} - \frac{\alpha_1 \left(C_{L,2} - C_{L,1}\right)}{\alpha_2 - \alpha_1}. \tag{8}$$

While the drag polar can be described as a second-order polynomial, not all polynomial coefficients need to be determined, as the polar is symmetric about the C_D-axis. Therefore, the second-order equation becomes:

$$p\left(x\right) = ax^2 + bx + c, \tag{9}$$

with the coefficient $b = 0$. As such, the drag polar can also be fit using two high-fidelity simulations, instead of the three needed for a general second-order polynomial. Therefore, the drag polar fit results in two equations with two unknowns (C_{D0} and k):

$$C_{D,1} = C_{D0} + kC_{L,1}^2 \tag{10}$$
$$C_{D,2} = C_{D0} + kC_{L,2}^2. \tag{11}$$

Finally, the resulting coefficients for the drag polar are:

$$k_{drag} = \frac{C_{D,2} - C_{D,1}}{C_{L,2}^2 - C_{L,1}^2} \tag{12}$$
$$C_{D0} = C_{D1} - k_{drag}C_{L,1}^2 \tag{13}$$

The analytical partial derivatives (see Appendix) provided for the polar fit process were verified using the complex step method and shown to be accurate to machine precision.

2.2 Transient Flight Mechanics

The transient mission analysis component of this work is enabled using the Dymos toolbox [16] and flight mechanics ordinary differential equations (ODE) for a point mass. The equations of motion (EOM) for the

transient flight mechanics as used by on Bryson [19] as well as Falck et al. [4] for a minimum time climb problem are:

$$\frac{dv}{dt} = \frac{T}{m}\cos\alpha - \frac{D}{m} - g\sin\gamma \tag{14}$$

$$\frac{d\gamma}{dt} = \frac{T}{mv}\sin\alpha + \frac{L}{mv} - \frac{g\cos\gamma}{v} \tag{15}$$

$$\frac{dh}{dt} = v\sin\gamma \tag{16}$$

$$\frac{dr}{dt} = v\cos\gamma \tag{17}$$

$$\frac{dm}{dt} = -\frac{T}{gI_{sp}} \tag{18}$$

As this work studies a hybrid electric power train and the time interval over which the analyses is conducted is relatively short, the change in mass due to fuel burn is assumed to be negligible and will therefore not be considered. The flight path angle, γ, will be used as a control rather than a state, thus further simplifying the EOM:

$$\frac{dv}{dt} = \frac{T}{m}\cos\alpha - \frac{D}{m} - g\sin\gamma \tag{19}$$

$$\frac{dh}{dt} = v\sin\gamma \tag{20}$$

$$\frac{dr}{dt} = v\cos\gamma \tag{21}$$

Because the flight path angle now is a control variable, the angle of attack becomes a dependent variable. It can be determined by treating the state rate equation from Equation 15 as a residual equation:

$$\mathcal{R} = \frac{T}{mv}\sin\alpha + \frac{L}{mv} - \frac{g\cos\gamma}{v}. \tag{22}$$

The residual equations,

$$\mathcal{R} = f\left(\alpha, \gamma, T, m, v, C_{L\alpha}, C_{L0}, g\right), \tag{23}$$

are a function of the angle of attack, flight path angle, thrust, vehicle mass, vehicle speed, lift slope, lift coefficient at $\alpha = 0$, and the gravitational acceleration. Being an implicit quantity, the angle of attack, α, is determined using a root-finding algorithm. Analytical partial derivatives of the residual function were derived and total derivatives for the optimizer are determined using Gaussian elimination (Direct Solver) in OpenMDAO.

The total ODE group for the aircraft mission analysis consists of the determination of the lift coefficient (implicit relationship described in Equation 22), drag coefficient, and aerodynamic forces, followed by an evaluation of the flight mechanics EOM. The flight path, γ, and the thrust, T, serve as control variables and are driven by the optimizer.

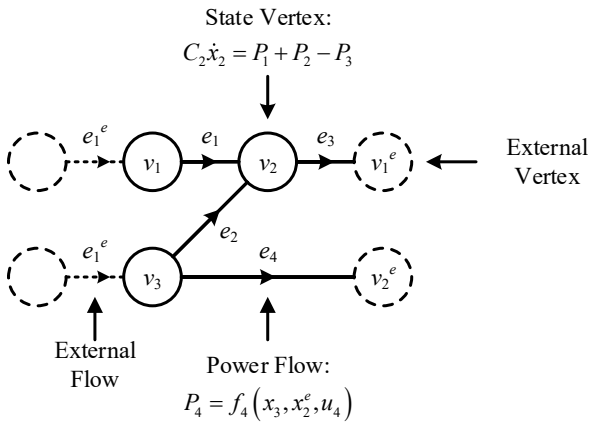

Figure 3: Notional representation of a graph model (modified from [23]).

2.3 Graph-Based Power and Thermal Subsystem Modeling

Graph-based models, which are based in conservation laws, are modular [20], computationally efficient [21], and effectively capture the dynamics of multi-domain systems [20, 22], which make it a useful framework for design optimization of power and thermal systems. The models described in the following sections are developed in a framework named Graphmos, which is based on the OpenMDAO and Dymos optimization framework. To enable gradient-based optimization, the Graphmos framework provides analytical partial derivatives for each system state and assembles the total derivatives using OpenMDAO's efficient derivative assembly routines. The following sections describe the graph-based model formulation and introduce the various component models used in this work.

Graph-based models capture conservation based dynamics with an oriented graph consisting of N_v vertices $v_i \in \mathcal{V} : i \in [1 : N_v]$ and N_e oriented edges $e_j \in \mathcal{E} : j \in [1 : N_e]$ as shown in Figure 3. Each edge e_j is oriented from a tail vertex v_j^{tail} to a head vertex v_j^{head}. Additionally, the set of edges entering and leaving a vertex v_i is given by $\mathcal{E}_i^{head} = \{e_j : v_j^{head} = v_i\}$ and $\mathcal{E}_i^{tail} = \{e_j : v_j^{tail} = v_i\}$, respectively.

In the graph-based models presented in this work, each vertex v_i represents an energy state x_i of the system and each edge e_j represents a power flow P_j (e.g. power) between adjacent vertices. Note that power can move in either direction along the edge, but the orientation defines the convention for positive power flow from v_j^{tail} to v_j^{head}. Based in conservation laws, the state dynamics of vertex v_i are given by

$$C_i \dot{x}_i = \sum_{\{j : e_j \in \mathcal{E}_i^{head}\}} P_j - \sum_{\{j : e_j \in \mathcal{E}_i^{tail}\}} P_j, \tag{24}$$

where $C_i \geq 0$ is the capacitance of the vertex v_i. The power flow along edge e_j is defined as

$$P_j = f_j\left(x_j^{tail}, x_j^{head}, u_j\right) \tag{25}$$

By observation, each edge power flow is a nonlinear function of adjacent vertex states and inputs u_j.

Disturbances and interactions with external systems such as the environment are captured through N_{ev} external vertices $v_i^e \in \mathcal{V} : i \in [1 : N_{ev}]$ and N_{ee} external edges $e_j^e : j \in [1 : N_{ee}]$ represented by the dashed circles and

edges in Figure 3. Each external vertex v_i^e and edge e_i^e are represented by external states x_i^e and power flows P_j^e, respectively.

The full graph model dynamics are compactly given by

$$C\dot{x} = -\bar{M}P + DP^e, \tag{26}$$

where $C \in \mathbb{R}^{(N_v - N_{ev}) \times (N_v - N_{ev})}$ is a diagonal matrix of vertex capacitances, x is the state vector, $\bar{M}$ is the graph's upper incidence matrix, $P = F\left(x, x^e, u\right)$ is a vector of power flows, D is the external edge incidence matrix, and P^e is a vector of external power flows. The incidence matrix $M = [m_{ij}] \in \mathbb{R}^{N_v \times N_e}$ of an oriented graph describes the graph's connectivity and is given by

$$m_{ij} = \begin{cases} 1 & \text{if } v_i \in \mathcal{E}_j^{tail}, \\ -1 & \text{if } v_i \in \mathcal{E}_j^{head}, \\ 0 & \text{else.} \end{cases} \tag{27}$$

The incidence matrix can be partitioned as

$$M = \begin{bmatrix} \bar{M} \\ \underline{M} \end{bmatrix} \text{ with } \bar{M} \in \mathbb{R}^{(N_v - N_t) \times N_e}, \tag{28}$$

where $\bar{M}$ relates power flows to states. Similarly, the external edge incidence matrix relates external power flows to states.

$$d_{ij} = \begin{cases} 1 & \text{if } v_i \text{ is the head of } e_j^e, \\ 0 & \text{else.} \end{cases} \tag{29}$$

In this work, the 8 components detailed in Figure 7 are modeled in the graph-based modeling framework to represent the dynamics of an aircraft power, propulsion, and thermal management system. For brevity, the component graph-based models are illustrated in Figure 4, and the reader is referred to [20, 22, 24] for model derivation and system model assembly details. The vertices in Figure 4 are color-coded to distinguish between different state dynamics.

2.4 Coupled Multidisciplinary Problem

Because the coupled analysis is transient, all analysis disciplines are combined into an ODE group (Figure 5) used in Dymos. The states for the coupled ODE are the power and thermal states, y_{PTMS}, and the flight dynamic states: r, h, v. The outputs for the ODE group are the associated state rates, required by Dymos to simulate the transient response. The ODE inputs include the polar fitting data and the PTMS design variables, x_{ptms}, as well as the vehicle weight m, which is constant for these studies, but may be determined outside of the ODE using Raymer weight equations [25] or similar. While the aerodynamic analysis is not a direct function of the aerodynamic design variables of the global problem, the polar fit data ($C_{L\alpha}$, etc.) couple the low-fidelity aerodynamics of the transient solution to the design variables of the higher-fidelity aerodynamic analysis.

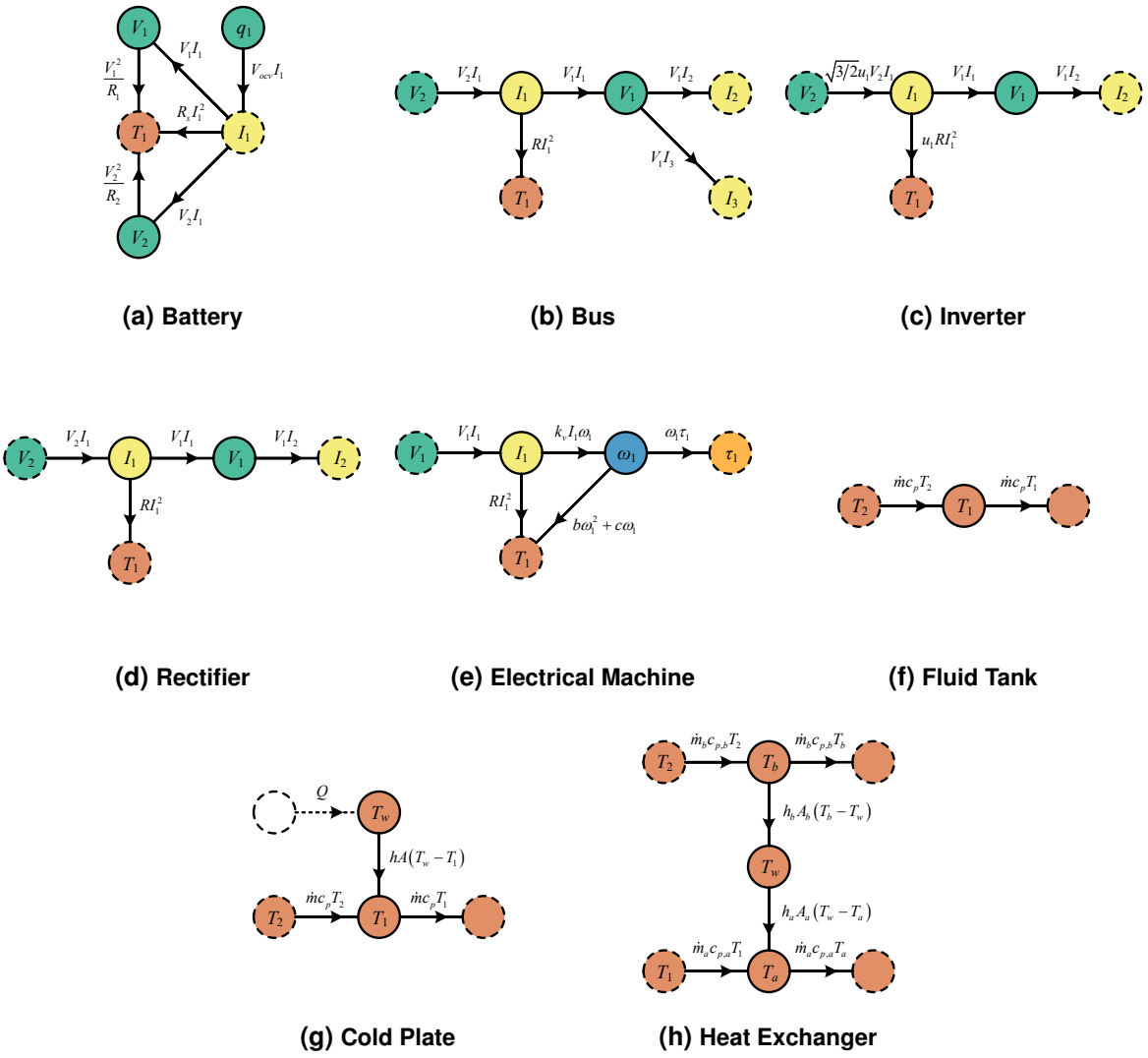

Figure 4: Graph model representations of PTMS components used in this work. The colors of the nodes correspond to: voltage, current, angular velocity, torque, and temperature.

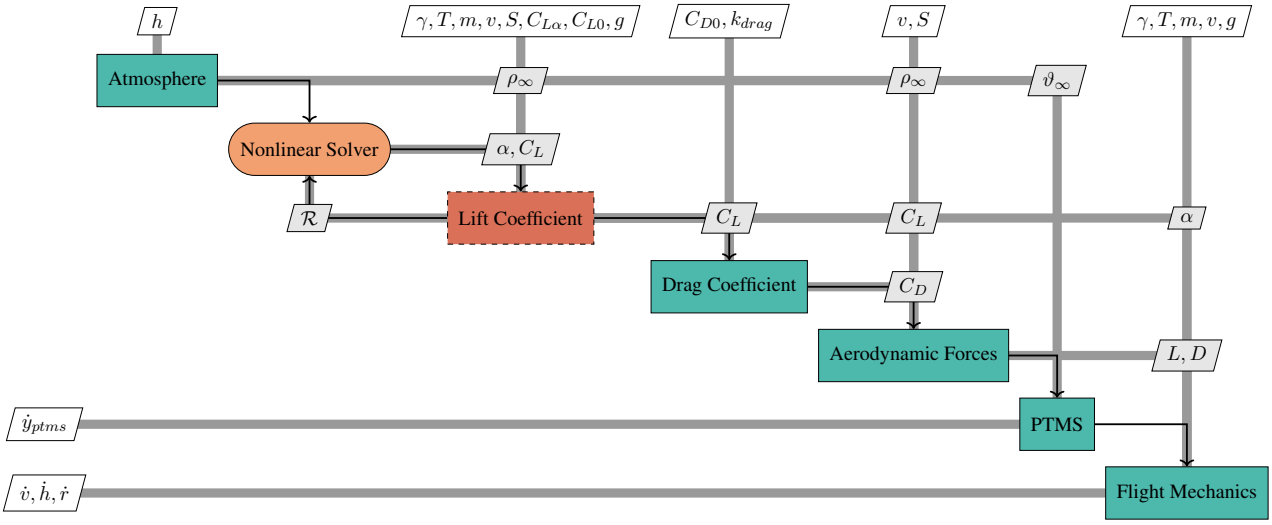

Figure 5: XDSM diagram of the coupled ODE group used in the dynamic optimization. The vehicle states (h, v, r) along with the PTMS states (y_{PTMS}) are provided by as inputs to the ODE and the group outputs their respective state rates. Note, the implicit lift coefficient component which provides both the lift coefficient and angle of attack, α as outputs. This component requires the atmospheric density as an input, as the residual equations contain the lift force.

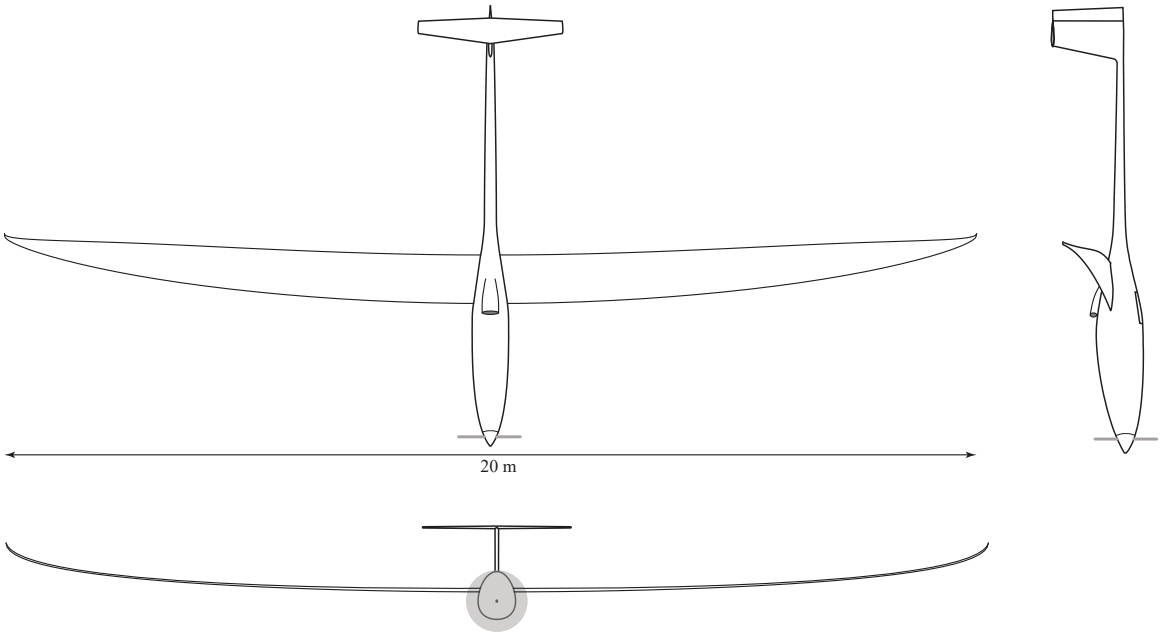

Figure 6: Geometry representation of the notional HALE aircraft baseline configuration including its power and thermal system.

3 MODEL DESCRIPTION

A notional high altitude long endurance (HALE) aircraft, *Explorer*, was created for the purposes of numerical studies within this work. The baseline wing planform is derived from an open-source sailplane model, while a serial hybrid architecture was created for the powertrain and PTMS subsystems. This section describes the numerical model used for the studies in this work.

3.1 Vehicle Configuration

The *Explorer* vehicle is based on the open-source OSM-2 sailplane, which was designed outside the scope of this work[1]. The OSM-2 is a notional twin-seat sailplane in the 20m class featuring a T-tail configuration, a single wheel main and tail gear (Figure 6). Furthermore, while the OSM-2 fuselage provides space in the fuselage for a collapsible propeller tower, the configuration was designed as a pure sailplane without an engine.

Explorer borrows its outer mold line (OML) from OSM-2, however, it replaces the cockpit with a compartment for a serial-hybrid powertrain, adding a propeller to the vehicle nose. While the OSM-2 features four flaperons across its half-span, control surfaces are not modeled on *Explorer* for these studies. The maximum take-off weight (MTOW) for *Explorer* is $850\,kg$ and while OSM-2 provides a parametric mass model based on Thomas [26], the vehicle mass remains constant and uncoupled to the design variables within this work.

[1]The Open Sailplane Models and the OSM-2 configuration were created outside of this work and will be publicly released in late 2022 as a git repository: `https://github.com/chrislupp/OpenSailplaneModels`

3.2 Wing Planform and Design Parameters

The *Explorer* HALE configuration borrows its wing planform from the OSM-2 wing. As such, it also inherits the OSM-2 geometric parameterization. The OSM-2 wing planform is the result of an aerodynamic shape optimization, minimizing drag, using a VLM solver:

$$\begin{aligned} &\text{minimize:} && C_D \\ &\text{with respect to:} && x = [c_i, x_{shear,i}, \theta_i]^T \\ &\text{subject to:} \\ & && C_L = 0.5 \\ & && S = 15.5 \\ & && b = 20.0 \end{aligned} \tag{30}$$

For this initial optimization problem the wing was parameterized with B-splines to control the chord distribution, c_i, the amount of mesh shear in x-direction (akin to a distributed sweep variable), x_{shear}, and the wing twist distribution, θ_i. The design was constrained by a required lift coefficient as well as the project wing surface area and wing span. The projected surface area constraint served in lieu of a strength constraint, as this constraint controls the maximum wing loading of the vehicle.

While all of OSM-2's parameters remain available in the optimization of the *Explorer* HALE vehicle, only the wing chord and x-shear control points are used within this work.

3.3 Propulsion, Power and Thermal Management Subsystems

The *Explorer* HALE is a single propeller aircraft driven by a series hybrid electric power and propulsion system consisting of power generation, energy storage, and thermal management components (Figure 7). In the power system, the battery provides electrical energy storage capacity and charges and discharges based on the vehicle's power requirements. The generator and passive rectifier are coupled to the aircraft's combustion engine to convert mechanical shaft power to electrical power that can recharge the battery or power the propulsion system. The electronic propulsion system consists of a controlled inverter and motor that is coupled to the propeller to generate thrust.

Inherent inefficiencies in the power system result in heat generation that, if not managed, would result in system failures. Therefore, the main heat generating components (inverter, motor, rectifier, and generator) are cooled by an active thermal management system (TMS). Cold plates conduct heat away from the electrical components into the working fluid of the thermal management system (Figure 7). While batteries produce heat in operational conditions, their thermal management—required in practice—was neglected within this work. The heat absorbed by the fluid is eventually rejected from the system through the heat exchanger that couples the thermal management system to the aircraft heat sink such as an air cycle machine or ram air. The fluid tank

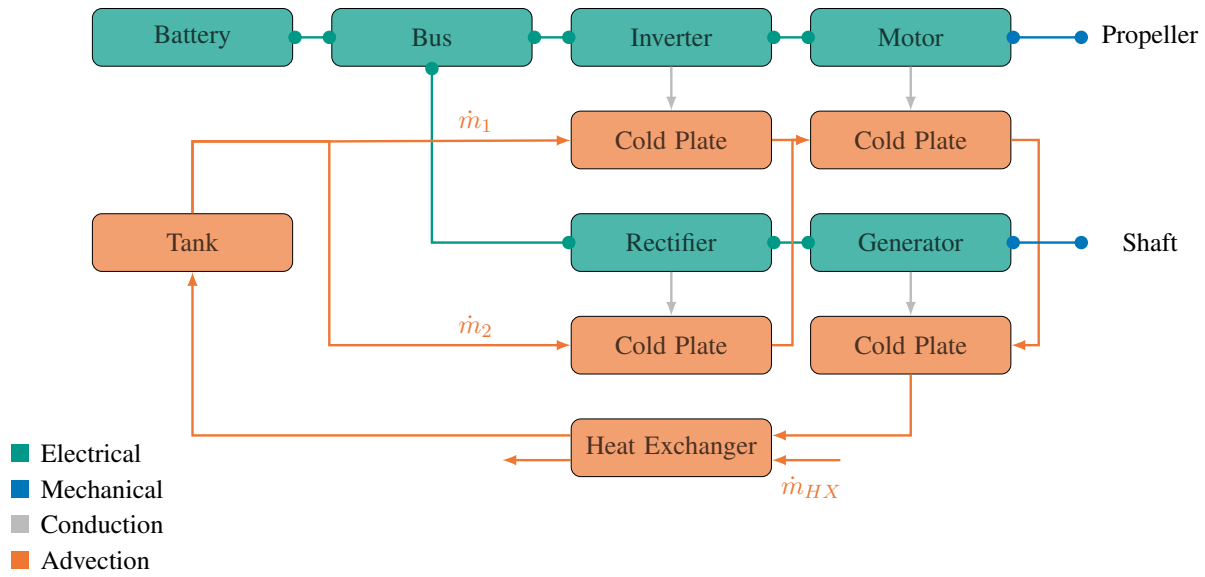

Figure 7: Serial hybrid propulsion system of the notional HALE aircraft including its power and thermal system.

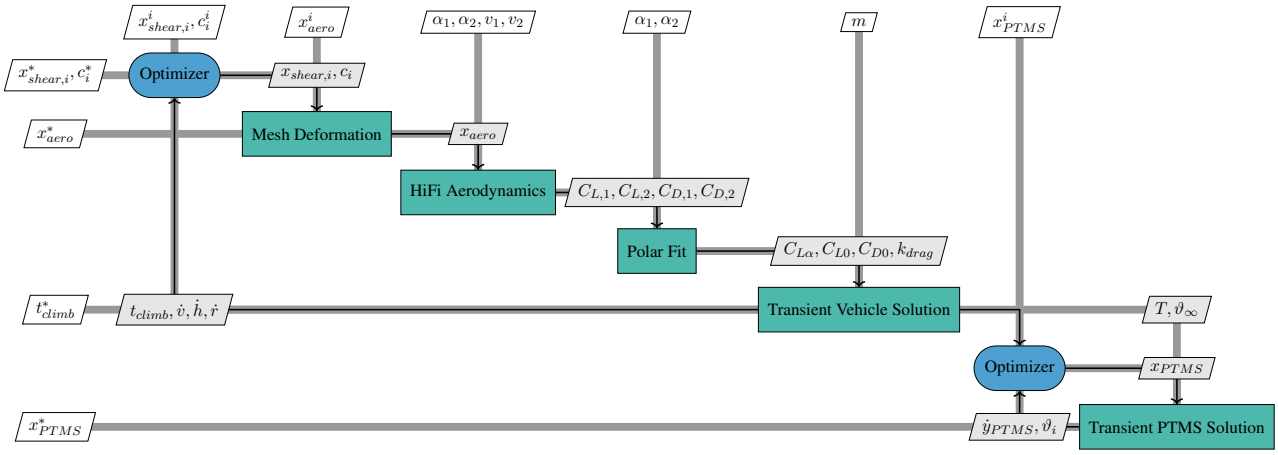

Figure 8: XDSM diagram of the sequential vehicle, mission, and PTMS optimization problem. After the successful vehicle optimization, the required thrust and ambient temperature profile are passed to the PTMS sizing problem.

stores coolant to increase the total thermal capacitance of the TMS. The fluid mass flow rate in each flow path is controlled by pumps to vary the amount of heat absorption and rejection.

4 NUMERICAL STUDIES

Two main optimization studies are conducted in this work: a sequential design of the vehicle and mission followed by the sizing of the PTMS subsystem (Figure 8), as well as a fully coupled, simultaneous optimization of the vehicle, mission, and PTMS system (Figure 1). The vehicle mission profile was simplified to a minimum time climb problem, with the vehicle climbing from 100 meters to 2500 meters altitude. Finally, analyses are conducted to quantify the accuracy and applicability of the low-fidelity aerodynamics model.

4.1 Sequential Design

The sequential design (Figure 8) consists of the vehicle and mission profile optimization followed by a PTMS system sizing. While these two optimizations can be automated to run sequentially (as depicted in Figure 8), in this study they were conducted separately.

Vehicle Shape and Trajectory Optimization

The vehicle shape and mission optimization in the sequential optimization studies consists of the multi-fidelity problem depicted in the first optimization block of Figure 8. The shape design variables for this problem directly affect the high-fidelity aerodynamic solution and indirectly influence the low-fidelity aerodynamics used in the transient trajectory analysis. In addition to the shape variables, the flight path angle and vehicle thrust serve

as control variables for the mission analysis. The objective function was chosen as a minimum time climb problem subject to trajectory constraints for the final conditions. Furthermore, path constraints are imposed on the vehicle speed and the horizontal acceleration, $\dot{v}$. The speed constraint ensures that the vehicle remains within its operational bounds, while the acceleration constraint prevent the optimizer from imposing unrealistic accelerations on the vehicle. The initial and final flight path angle rates were constrained to zero. Additionally, a wing area constraint was added to prevent extremely low surface areas to achieve higher aspect ratios. Finally, the flight path angle and thrust (control variables) are controlled via B-Splines to reduce the number of design variables. The optimization problem, without the design variables and constraints imposed by the transient solution, can be written as:

$$
\begin{aligned}
&\text{minimize:} && t_{climb} \\
&\text{with respect to:} && \mathrm{x} = [c_i, x_{shear,i}, \gamma_i, T_i]^T \\
&\text{subject to:} && \\
& && h\left(t_0\right) = 100m \qquad h\left(t_{end}\right) = 2500m \\
& && \gamma\left(t_0\right) = 0 \qquad\quad \gamma\left(t_{end}\right) = 0 \\
& && v\left(t_0\right) = 30\frac{m}{s} \qquad v\left(t_{end}\right) = 30\frac{m}{s} \\
& && S \geq 14.0\, m^2 \\
& && v \leq 80\frac{m}{s} \\
& && \dot{v} \leq 3.0\frac{m}{s^2}
\end{aligned}
\tag{31}
$$

While this problem statement may at first glance appear to be comparatively small, the implicit transient solution increases the problem size substantially by adding the states as variables as well as constraints for the defect rates.

The optimization problem was solved using SciPy optimize's SLSQP [27] algorithm and the vehicle state and control variable trajectories as well as the resulting wing planform are depicted in Figure 9. At the beginning of the climb profile the vehicle increases its speed before transitioning to steady climb, during which the speed decreases. Some oscillation is observed in the flight path angle as the vehicle builds up speed before converting it into potential energy by climbing. Towards the end of the climb segment, the flight path angle continually decreases as the thrust decreases to zero and the vehicle reaches its target altitude. The optimum wing planform retains the general shape of the OSM-2, while decreasing the projected surface area (Figure 9). This is noteworthy, as the baseline planform resulted from an aerodynamic optimization.

PTMS Sizing

Following the vehicle and mission sizing, the PTMS can be optimized. The ambient temperature profile is taken from the vehicle optimization, as this affects the ability of the heat exchanger to reject heat from the system. The system thrust is constrained to the maximum required thrust required during the vehicle's trajectory. The objective function for the PTMS sizing is the integrated mass flow of the coolant loop, effectively minimizing

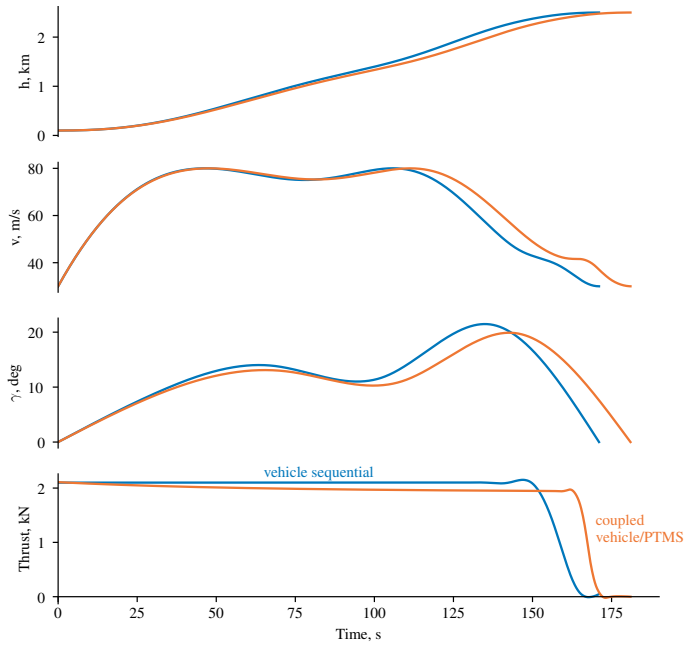

(a) Vehicle trajectory and control variables

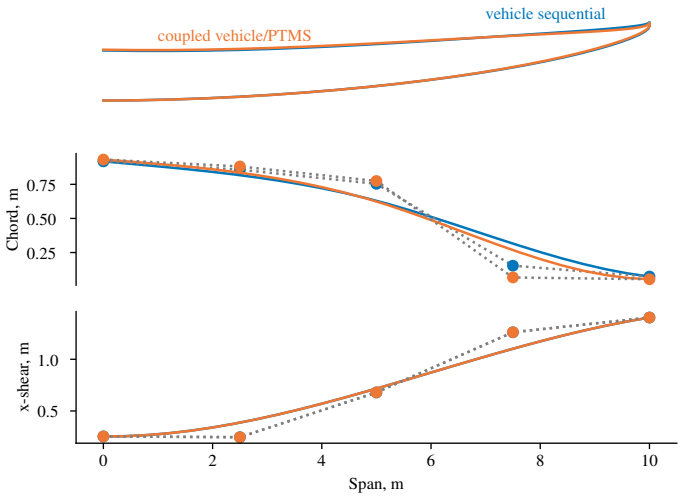

(b) Vehicle planform

Figure 9: Results for the vehicle shape and mission design from the sequential and coupled design studies.

the required cooling effort. The electrical component cold plate dimensions serve as design variables, along with the duty cycle, generator torque, and coolant flow rates. Finally, temperature constraints are imposed on the individual PTMS components to maintain operational limits. The entire problem statement is:

$$\begin{aligned}
&\text{minimize:} && \int_{t_0}^{t_f} \dot{m}\,\mathrm{dt} \\
&\text{with respect to:} && x = [x_{PTMS}, \eta, \tau_{gen}, \dot{m}_1, \dot{m}_2, \dot{m}_{HX}]^T \\
&\text{subject to:} && \\
& && T = T_{max}^{vehicle} \\
& && \vartheta_i = \vartheta_{max,i}
\end{aligned} \tag{32}$$

The resulting optimally sized coldplate and heat exchanger dimensions are shown in Figure 11, while the state and control variables for the problem are shown in Figure 10.

4.2 Coupled Design

The coupled design problem follows the methodology laid out in Figure 1. The vehicle, mission, and PTMS subsystem are sized simultaneously, allowing for design trade-offs during the optimization process. The number of design variables increases by combining the vehicle sizing with the PTMS variables (sizes of coldplates and the thermal tank). As such, the coupled optimization problem statement is:

$$\begin{aligned}
&\text{minimize:} && t_{climb} \\
&\text{with respect to:} && x = [c_i, x_{shear,i}, \gamma_i, x_{PTMS}, \eta, \tau_{gen}, \dot{m}_1, \dot{m}_2, \dot{m}_{HX}]^T \\
&\text{subject to:} && \\
& && h\left(t_0\right) = 100m \qquad h\left(t_{end}\right) = 2500m \\
& && \gamma\left(t_0\right) = 0 \qquad \gamma\left(t_{end}\right) = 0 \\
& && v\left(t_0\right) = 30\frac{m}{s} \qquad v\left(t_{end}\right) = 30\frac{m}{s} \\
& && S \geq 14.0\,m^2 \\
& && v \leq 80\frac{m}{s} \\
& && \dot{v} \leq 3.0\frac{m}{s^2} \\
& && \vartheta_i = \vartheta_{max,i}
\end{aligned} \tag{33}$$

The trajectory and geometry of the coupled optimization results are shown in Figure 9, while the thermal states and controls are shown in Figure 10. Finally, the PTMS component dimensions are shown in Figure

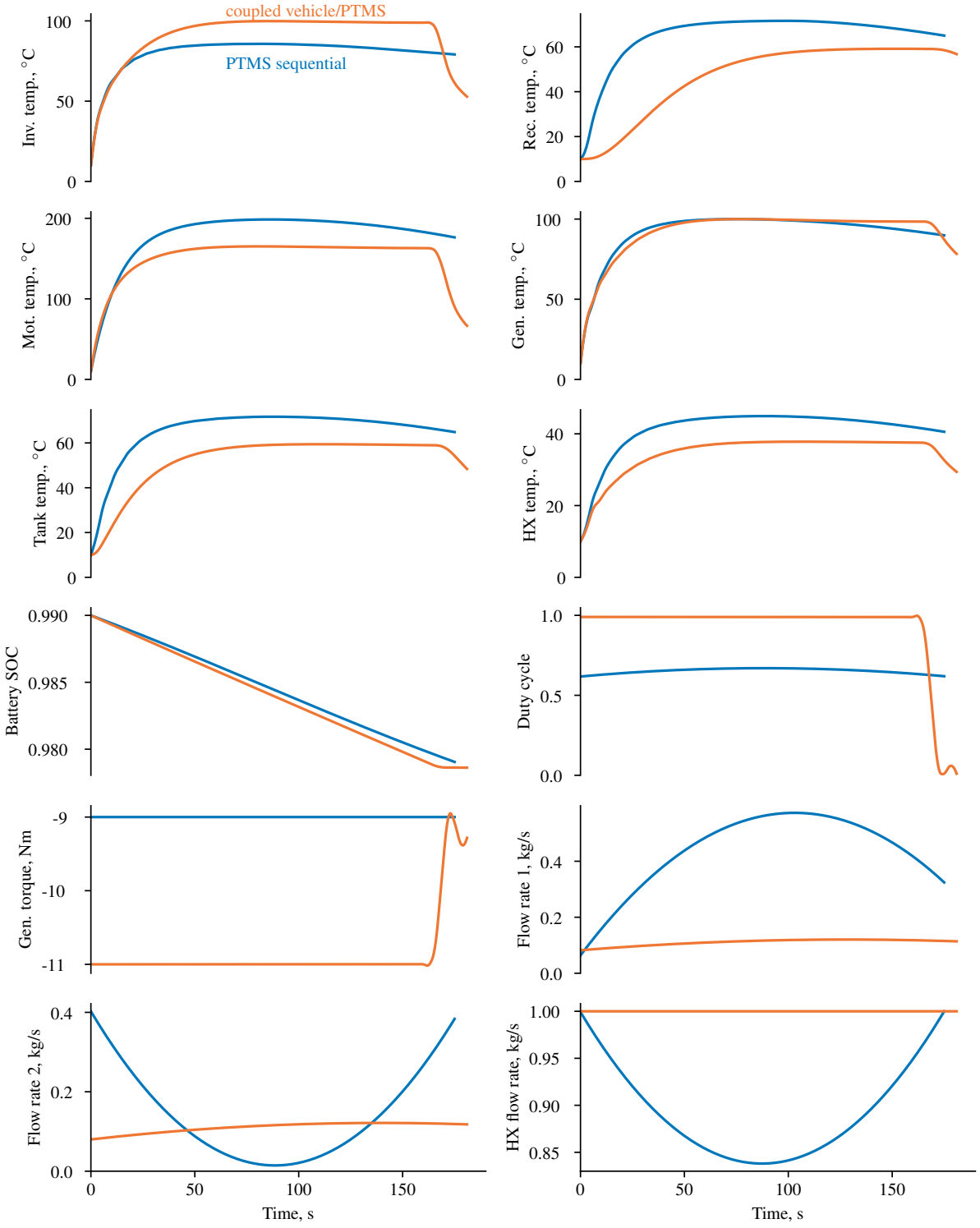

Figure 10: Thermal state and control variable trajectories for the PTMS subsystem optimized during the sequential and coupled design processes.

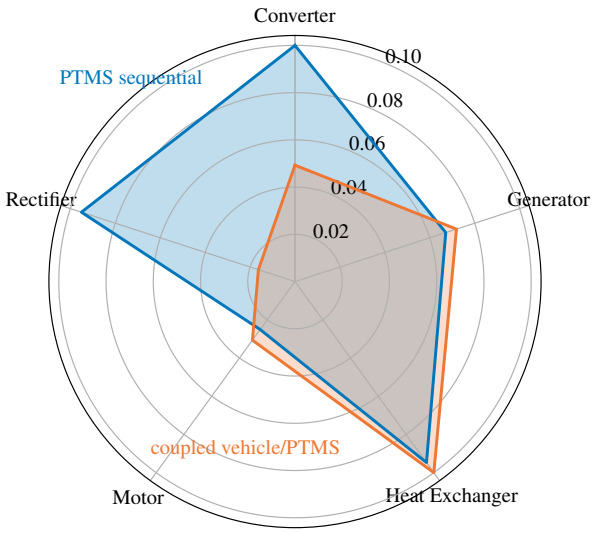

Figure 11: Coldplate and heat exchanger dimensions (in meters) for the sequential PTMS and coupled designs.

11. Noticeably, the PTMS components are sized differently than the sequential design, resulting in substantially smaller cold plate dimensions. The coupled nature of the problem is also reflected in the temperature profiles, with a reduction in thrust driving a drop in component temperatures towards the end of the mission profile. While some component temperatures of the coupled design are lower than the sequential configuration, the sequential vehicle design (without thermal constraints) performs the climb slightly faster than the coupled solution. Of note, the coupled design slowly reduces thrust over its flight profile compared to a constant thrust for the sequential design. The vehicle planform is similar to the sequential design. It does, however, feature a slightly larger chord distribution inboard, with a smaller wing tip footprint, to achieve the minimum surface area constraint. Noticeably, the thermal control variables and states differ from the sequential design emphasizing the need for a tightly coupled flight mechanics and thermal analysis.

4.3 Accuracy of the Multi-Fidelity Approach

Finally, the validity of the previous optimization studies largely depends on the accuracy of the low-fidelity aerodynamic models generated during the polar fitting. To assess the correlation between the fitted polar coefficients and the higher-fidelity VLM solution, an angle of attack sweep of the VLM solution was conducted and the data plotted over the analytical lift curve and drag polar (Figure 12).

By visual inspection of Figure 12a, the lift curve shows a close correlation to the data obtained by the VLM, which is confirmed by relative errors beneath 0.1 percent (Figure 12c). It should be noted, that the error increases as the angle of attack approaches zero. This is a result of the relative error metric, which is unbounded for this value.

While the analytical drag polar shows good agreement (Figure 12b) to the VLM data, the relative error is approx. an order of magnitude larger. Despite this, the largest relative error encountered is still smaller than one percent. Naturally, the low-fidelity solution is exact at both of the operating points used to fit the lift curve and the drag polar.

The high degree of accuracy of the low-fidelity solution follows from the nature of the high-fidelity solution (VLM) used in this work. As the VLM solution is based on potential flow assumptions, the lift curve is linear and the drag polar closely follows a second-order polynomial. Should the high-fidelity solution be replaced with a viscous solution, such as Reynolds Averaged Navier-Stokes (RANS) CFD, neither the lift curve, nor the drag polar approximation would be valid across the entire operational spectrum. In that case, alternative low-fidelity representations with an appropriate reduction process need to be chosen.

5 CONCLUDING REMARKS

This paper described a multi-fidelity approach to coupled sizing of vehicle shape, its mission, and its PTMS subsystem given trajectory and thermal constraints. This works primary contributions are:

- to establish a method for including gradient-based shape optimization when conducting transient mission analyses

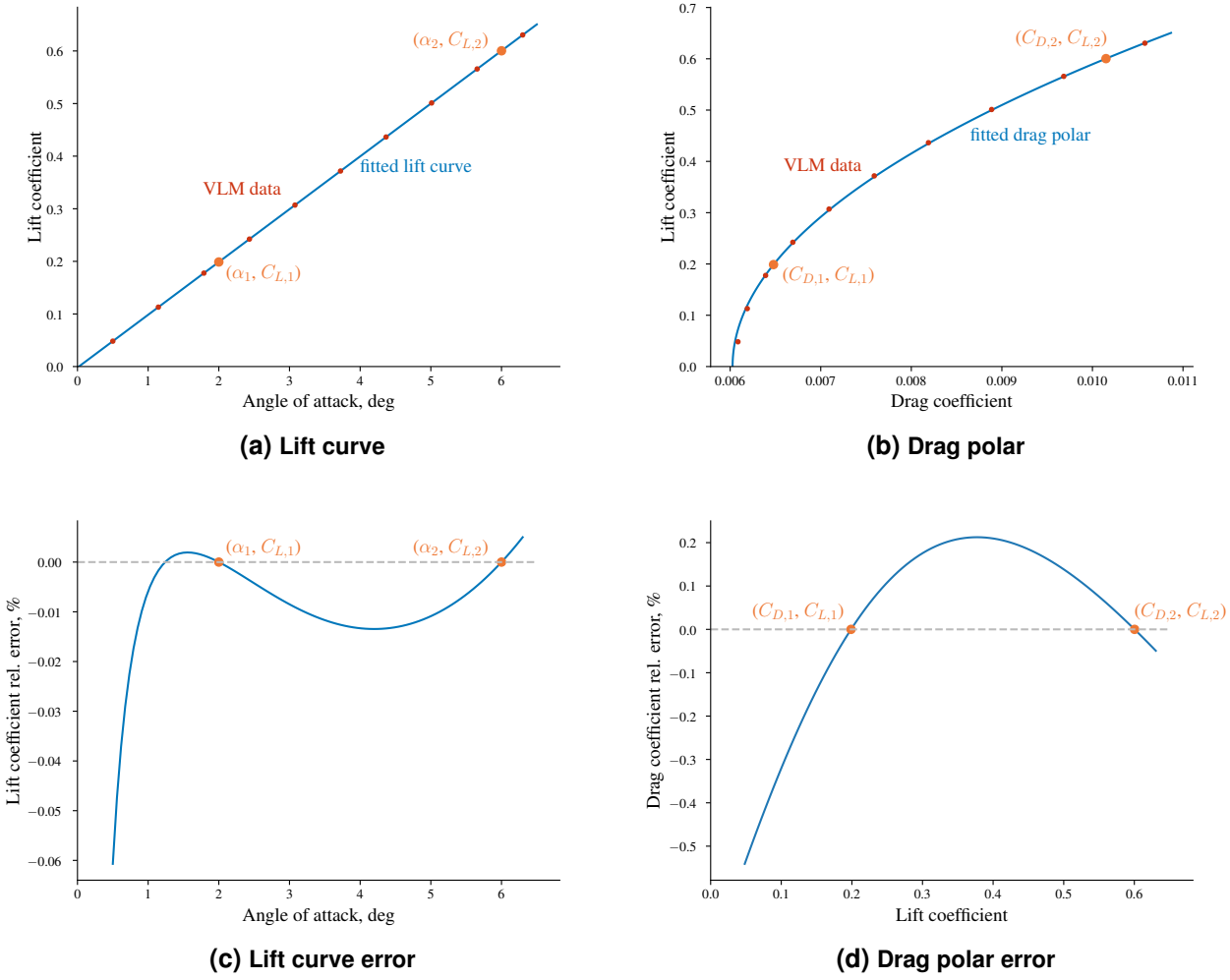

(a) Lift curve

(b) Drag polar

(c) Lift curve error

(d) Drag polar error

Figure 12: Accuracy of the low-fidelity aerodynamic model compared to the higher-fidelity VLM solution for the baseline *Explorer* vehicle. While the low-fidelity aerodynamic solution is exact at the operating points used to create the lift curve and polar fit, an error is incurred outside these points. However, the relative error for both the lift curve and drag polar remain below one percent.

- to demonstrate a gradient-based PTMS framework capable of modeling complex systems within a coupled MDO problem.

The methods and tools developed within this work were demonstrated on a simple, notional HALE aircraft in a coupled vehicle, mission, and PTMS subsystem optimization. The sequential design of the vehicle and mission as well as the PTMS were conducted and serve as a reference to the coupled results. It is noteworthy, that the fully coupled solution resulted in a lower performing objective function value, indicating that the vehicle is limited by it's thermal performance. This underscores the need to include coupled analyses for potentially thermally constrained vehicles.

Finally, the accuracy of the multi-fidelity approach was assessed compared to the higher-fidelity VLM solution. Due to the potential flow assumptions underpinning the VLM analysis, the low-fidelity aerodynamic model was near exact. Despite VLM models being widely used in conceptual design, future work should determine the need to adjust the polar fitting methodology to accommodate CFD analyses. Nonetheless, the multi-fidelity approach presented in this work, enables a more detailed method of shape optimization of transient problems while offering a path for expanding towards higher levels of aerodynamic fidelity.

6 REFERENCES

[1] Jasa, J. P., Mader, C. A., and Martins, J. R. R. A., Trajectory Optimization of a Supersonic Aircraft with a Thermal Fuel Management System, in 2018 Multidisciplinary Analysis and Optimization Conference, pp. 1–16, American Institute of Aeronautics and Astronautics, Atlanta, Georgia, June 2018, ISBN 978-1-62410-550-0.

[2] Bergholz, R., and Hitch, B., Thermal management systems for high Mach airbreathing propulsion, in 30th Aerospace Sciences Meeting and Exhibit, American Institute of Aeronautics and Astronautics, Reno,NV,U.S.A., January 1992.

[3] Doman, D. B., Rapid Mission Planning for Aircraft Thermal Management, in AIAA Guidance, Navigation, and Control Conference, American Institute of Aeronautics and Astronautics, Kissimmee, Florida, January 2015, ISBN 978-1-62410-339-1.

[4] Falck, R. D., Chin, J., Schnulo, S. L., Burt, J. M., and Gray, J. S., Trajectory Optimization of Electric Aircraft Subject to Subsystem Thermal Constraints, in 18th AIAA/ISSMO Multidisciplinary Analysis and Optimization Conference, American Institute of Aeronautics and Astronautics, Denver, Colorado, June 2017, ISBN 978-1-62410-507-4.

[5] Alyanak, E. J., and Allison, D. L., Fuel Thermal Management System Consideration in Conceptual Design Sizing, in 57th AIAA/ASCE/AHS/ASC Structures, Structural Dynamics, and Materials Conference, American Institute of Aeronautics and Astronautics, San Diego, California, USA, January 2016, ISBN 978-1-62410-392-6.

[6] Clark, D. L., and Abolmoali, P. C., Gradient-Based Optimization of Time-Dependent Aircraft Subsystems under Uncertainty, pp. 1–14, American Institute of Aeronautics and Astronautics, Virtual Event, August 2021, ISBN 978-1-62410-610-1.

[7] Herman, A. L., and Conway, B. A., Direct optimization using collocation based on high-order Gauss-Lobatto quadrature rules, Journal of Guidance, Control, and Dynamics, 19(3):pp. 592–599, May 1996.

[8] Garg, D., Patterson, M., Darby, C., Francolin, C., Huntington, G., Hager, W., and Rao, A., Direct Trajectory Optimization and Costate Estimation of General Optimal Control Problems Using a Radau Pseudospectral Method, in AIAA Guidance, Navigation, and Control Conference, pp. 1–29, American Institute of Aeronautics and Astronautics, Chicago, Illinois, August 2009, ISBN 978-1-60086-978-5.

[9] Falck, R. D., Ingraham, D., and Aretskin-Hariton, E., Multidisciplinary Optimization of Urban-Air-Mobility Class Aircraft Trajectories with Acoustic Constraints, in 2018 AIAA/IEEE Electric Aircraft Technologies Symposium, pp. 1–7, American Institute of Aeronautics and Astronautics, Cincinnati, Ohio, July 2018, ISBN 978-1-62410-572-2.

[10] Schnulo, S. L., Chin, J., Falck, R. D., Gray, J. S., Papathakis, K. V., Clarke, S. C., Reid, N., and Borer, N. K., Development of a Multi-Segment Mission Planning Tool for SCEPTOR X-57, in 2018 Multidisciplinary Analysis and Optimization Conference, American Institute of Aeronautics and Astronautics, Atlanta, Georgia, June 2018, ISBN 978-1-62410-550-0.

[11] Falck, R. D., and Gray, J. S., Optimal Control within the Context of Multidisciplinary Design, Analysis, and Optimization, in AIAA Scitech 2019 Forum, pp. 1–17, American Institute of Aeronautics and Astronautics, San Diego, California, January 2019, ISBN 978-1-62410-578-4.

[12] Malcolm, D. J., and Laird, D. L., Extraction of equivalent beam properties from blade models, Wind Energy, 10(2):pp. 135–157, March 2007.

[13] Stodieck, O., Cooper, J. E., Neild, S. A., Lowenberg, M. H., and Iorga, L., Slender-Wing Beam Reduction Method for Gradient-Based Aeroelastic Design Optimization, AIAA Journal, 56(11):pp. 4529–4545, November 2018.

[14] Lupp, C. A., and Cesnik, C. E. S., Including Geometrically Nonlinear Flutter Constraints in High-Fidelity Aircraft Optimization, in International Forum on Aeroelasticity and Structural Dynamics, pp. 1–18, Savannah, GA, June 2019.

[15] Gray, J. S., Hwang, J. T., Martins, J. R. R. A., Moore, K. T., and Naylor, B. A., OpenMDAO: an open-source framework for multidisciplinary design, analysis, and optimization, Structural and Multidisciplinary Optimization, 59(4):pp. 1075–1104, April 2019.

[16] Falck, R., Gray, J. S., Ponnapalli, K., and Wright, T., dymos: A Python package for optimal control of multidisciplinary systems, Journal of Open Source Software, 6(59):p. 2809, 2021, publisher: The Open Journal.

[17] Lambe, A. B., and Martins, J. R. R. A., Extensions to the design structure matrix for the description of multidisciplinary design, analysis, and optimization processes, Structural and Multidisciplinary Optimization, 46:pp. 273–284, 2012.

[18] Jasa, J. P., Hwang, J. T., and Martins, J. R. R. A., Open-source coupled aerostructural optimization using Python, Structural and Multidisciplinary Optimization, 57(4):pp. 1815–1827, April 2018.

[19] Bryson, A. E., Dynamic Optimization, Addison Wesley Longman, Menlo Park, CA, 1 edition, 1999, ISBN 0-201-59790-X.

[20] Aksland, C. T., and Alleyne, A. G., Hierarchical model-based predictive controller for a hybrid UAV powertrain, Control Engineering Practice, 115:pp. 1–15, October 2021.

[21] Russell, K. M., Aksland, C. T., and Alleyne, A. G., Graph-Based Dynamic Modeling of Two-Phase Heat Exchangers in Vapor Compression Systems, International Journal of Refrigeration, 137(March):pp. 244–256, 2022, publisher: Elsevier B.V.

[22] Koeln, J. P., Williams, M. A., Pangborn, H. C., and Alleyne, A. G., Experimental Validation of Graph-Based Modeling for Thermal Fluid Power Flow Systems, ASME 2016 Dyn. Syst. Control Conf, 2016.

[23] Pangborn, H. C., Hierarchical control for multi-domain coordination of vehicle energy systems with switched dynamics, Ph.D. thesis, University of Illinois Urbana-Champaign, Urbana, IL, 2019.

[24] Aksland, C. T., Modular modeling and control of a hybrid unmanned aerial vehicle's powertrain, Ph.D. thesis, University of Illinois Urbana Champaign, Urbana, IL, 2019.

[25] Raymer, D., Aircraft design: A conceptual approach, AIAA education series, American Institute of Aeronautics and Astronautics, Incorporated, 2018, ISBN 978-1-62410-490-9, tex.lccn: 2018033769.

[26] Thomas, F., and Milgram, J., Fundamentals of Sailplane Design, College Park Press, College Park, MD, 1999, ISBN 978-0-9669553-0-9.

[27] Jones, E., Oliphant, T., Peterson, P., and others, SciPy: Open source scientific tools for Python, 2001.